Observation of Quantum Confinement in Monodisperse Methylammonium Lead Halide Perovskite Nanocrystals Embedded in Mesoporous Silica

Victor Malgras,[†] Satoshi Tominaka,[†] James W. Ryan,[‡] Joel Henzie,[†] Toshiaki Takei,[†] Koji Ohara,[§] and Yusuke Yamauchi*,[†]

[†]World Premier International (WPI) Research Center for Materials Nanoarchitectonics, National Institute for Materials Science (NIMS), 1-1 Namiki, Tsukuba, Ibaraki 305-0044, Japan

[‡]International Center for Young Scientists (ICYS), National Institute for Materials Science (NIMS), 1-1 Namiki, Tsukuba, Ibaraki 305-0044, Japan

[§]Research and Utilization Division, Japan Synchrotron Radiation Research Institute, 1-1-1 Kouto, Sayo-cho, Sayo-gun, Hyogo 679-5198, Japan

S *Supporting Information*

ABSTRACT: Hybrid organic−inorganic metal halide perovskites have fascinating electronic properties and have already been implemented in various devices. Although the behavior of bulk metal halide perovskites has been widely studied, the properties of perovskite nanocrystals are less well-understood because synthesizing them is still very challenging, in part because of stability. Here we demonstrate a simple and versatile method to grow monodisperse $CH_3NH_3PbBr_xI_{x-3}$ perovskite nanocrystals inside mesoporous silica templates. The size of the nanocrystal is governed by the pore size of the templates (3.3, 3.7, 4.2, 6.2, and 7.1 nm). In-depth structural analysis shows that the nanocrystals maintain the perovskite crystal structure, but it is slightly distorted. Quantum confinement was observed by tuning the size of the particles via the template. This approach provides an additional route to tune the optical bandgap of the nanocrystal. The level of quantum confinement was modeled taking into account the dimensions of the rod-shaped nanocrystals and their close packing inside the channels of the template. Photoluminescence measurements on CH_3NH_3PbBr clearly show a shift from green to blue as the pore size is decreased. Synthesizing perovskite nanostructures in templates improves their stability and enables tunable electronic properties via quantum confinement. These structures may be useful as reference materials for comparison with other perovskites, or as functional materials in all solid-state light-emitting diodes.
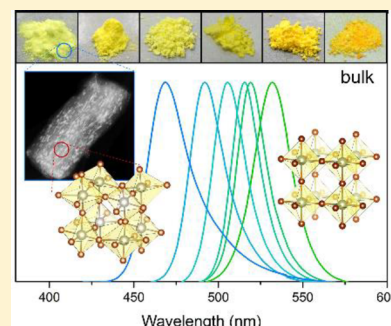
■ INTRODUCTION

Hybrid organic−inorganic metal halide perovskites exhibit unusual electronic, optical, and crystallographic properties enabling high mobilities[1,2] and long diffusion lengths.[3,4] They are promising candidates for photovoltaic applications and have rapidly achieved outstanding performances.[5−9] The chemical structure obeys the AMX_3 stoichiometry, where A is the organic cation, M is the metal cation (e.g., Pb^{2+}, Sn^{2+}), and X is the halide anion (e.g., Cl^-, Br^-, I^-). The optical bandgap can be tuned by selecting the appropriate A and X components: methylammonium and bromide lead to wider bandgaps than formamidinium and iodide, respectively.[10] While mixing bromide and iodide offers good control over the absorption band edge, these intermediate compositions can decrease the overall stability because they induce structural hindrances and are prone to the formation of microdomains.[11]

While numerous studies on bulk lead halide perovskites exist in the literature, less attention has been directed toward the synthesis and properties of $CH_3NH_3PbX_3$ quantum dots. The ability to tune the optical response of perovskites by altering their size or surface chemistry is useful for various light-emitting applications (e.g., LEDs, lasers). In addition, quantum confinement offers a different angle from which the electronic properties can be studied and manipulated. Many semiconductor nanocrystals display interesting behavior when their radius is less than the exciton Bohr radius, such as bandgap expansion, increased Coulombic attraction of the paired charges, energy level quantization, and slower electron−phonon relaxation.[12−15]

Research on $CH_3NH_3PbX_3$ nanocrystals has been primarily limited to colloidal nanoplatelets[16−19] and nanoparticles,[20−23] through coprecipitation or seeding methods, as well as encapsulation in alumina.[24] Not only are these materials difficult to obtain (e.g., multiple steps, use of chemical vapor deposition, separation), but they also typically yield small amounts of material. In addition, the optical properties of the material can become difficult to assess and separate from the

localized surface states induced by organic ligands. Compared to PbSe, InSb, or even CdSe, the exciton Bohr radius of $CH_3NH_3PbX_3$ is rather small ($r \sim 20$ Å),[25] and thus quantum confinement will only be observed for crystals with a radius much smaller than 5 nm.

We used highly ordered mesoporous materials as templates to guide the confined growth of nanoparticles and keep them isolated from each other. Over the last three decades, zeolites and mesoporous templates have been used to synthesize inorganic nanoparticles such as metals, oxides, carbons, or semiconductors with simple compositions in order to study their catalytic, magnetic, and optical properties.[26−33] $LaCoO_3$ and $LaNiO_3$ perovskites have been synthesized in mesoporous silica by impregnating them with aqueous solution of metal salts followed by calcination.[34,35] Here, we synthesized $CH_3NH_3PbBr_xI_{3-x}$ perovskite (with x = 0, 1, 2, 3) inside mesoporous silica templates to produce monodisperse 0D and 1D nanocrystals. Each template in this work is characterized by a specific pore size, limiting the crystal growth to a specific particle size, thus allowing us to control the level of confinement. We used mesoporous silica matrices having pores of diameters $d_{pore} \approx 7.1, 6.2, 4.2, 3.7$, and 3.3 nm. The N_2 adsorption/desorption isotherm data along with the calculated pore size distribution and small-angle X-ray scattering (SAXS) for each mesoporous silica template can be found in Figure S1. Our method uses capillary forces to fill the templates. Because of the relatively low interfacial surface tension between N,N-dimethylformamide (DMF) and silica, the dissolved perovskite precursors can be carried inside the channels with minimal resistance. Additionally, the chemistry underlying the formation of perovskite crystals does not involve the formation of any side-products that might require subsequent extraction. Crystallization of nanocrystals is induced by gradual supersaturation as the solvent evaporates. This method offers a simple, rapid, high-yield route to generate embedded perovskite quantum dots with accurate control over the crystal size.

■ EXPERIMENTAL METHODS

Materials. Lead iodide (PbI_2, ≥99.0%) and lead bromide ($PbBr_2$, ≥98.0%) were purchased from Sigma-Aldrich, and hydroiodic acid (HI, 57% in water), hydrobromic acid (HBr, 48% in water), methylamine (MA, 40% in methanol solution), and N,N-dimethylformamide (DMF, ≥ 99.7%) were acquired from Wako Pure Chemical Industries, Ltd. The chemicals were used without further purifications.

Precursors Synthesis. The methylammonium iodide/bromide (MAX, X = I, Br) was prepared by mixing equimolar ratios of MA solution and HI or HBr under constant argon flow, with the flask sitting in an ice bath for 2 h. The precipitate was rinsed with diethyl ether three times and recrystallized from ethanol. Before use, MAX was left overnight in a vacuum oven at 60 °C. Each composition was prepared by mixing an equimolar ratio of MAX and PbX_2 (i.e., x = 0, MAI + PbI_2; x = 1, MABr + PbI_2; x = 2, MAI + $PbBr_2$; x = 3, MABr + $PbBr_2$) in DMF. The concentration was 0.5 M for x = 0 and 1 and 0.2 M for x = 2 and 3.

Powder Preparation. The mesoporous silica powders with different pores of diameters $d_{pore} \approx 7.1, 6.2, 4.2, 3.7$, and 3.3 nm were synthesized according to previously published methods,[36,37] and the organic template was removed by calcination treatment at 500 °C for 6 h. The silica powders were dried overnight under vacuum at 80 °C before use. A 20 μL portion of each perovskite precursor was added dropwise to 40 mg of each mesoporous silica followed by vortex mixing for 30 min. The powders were then dried on a hot plate at 95 °C for 30 min before further characterization. Bulk perovskite used as a control sample was prepared by mixing the perovskite solution with nonporous silica nanospheres (~350 nm), which were found to

promote the photoluminescence properties when compared to the bare polycrystalline bulk.

Structural Analysis. The wide-angle powder X-ray diffraction patterns (PXRD) were obtained with a Rigaku Rint 2500 diffractometer with monochromated Cu Kα radiation at a rate of 0.2° min^{-1}. The high-resolution transmission electron microscope (HR-TEM) and scanning transmission electron microscope high-angle annular dark-field (STEM HAADF) images were obtained with a JEM-2100F TEM (JEOL, Japan) operated at an accelerating voltage of 200 kV with a spot size of 0.7 nm. Low-angle XRD profiles were acquired on a NANO VIEWER (Rigaku, Japan) equipped with a Micro Max-007 HF high-intensity microfocus rotating anode X-ray generator. X-ray total scattering data for obtaining pair distribution functions (PDFs)[38] were collected on a Rigaku R-AXIS imaging plate detector at the BL04B2 beamline of SPring-8 at a beam energy of 61.39 keV (λ = 0.20196 Å). Details are available in the Supporting Information. The energy dispersive X-ray spectroscopy (EDX) was performed using a Hitachi FE-SEM S-4800 with an accelerating voltage of 15 kV. The nitrogen adsorption−desorption isotherms were obtained with a high-precision Belsorp-mini apparatus (Bel Japan, Inc.) at 77 K, and the Barrett−Joyner−Halenda (BJH) method was used to calculate the pore size distribution of each silica template.[39,40]

Optical Measurements. The UV−vis−NIR absorption spectra of the solid powders were calculated from the reflectance spectra obtained on a JASCO V-570 at a scan rate of 400 nm min^{-1} from 220 to 1000 nm using a deuterium or halogen lamp as a light source (for the 220−350 nm range and 350−1000 nm range, respectively). Photoluminescence (PL) spectroscopy was performed on a JASCO FP8500 at a scan rate of 500 nm min^{-1}, with 10 nm slits. The photographs of the fluorescing powders were obtained under an AS ONE SLUV-8 UV lamp emitting at 254 nm. The PL lifetime measurements were carried out on a Hamamatsu Photonics Quantaurus-Tau at an excitation wavelength λ_{ex} = 365 nm. Absolute quantum yield (QY) measurements were performed on a Hamamatsu Photonics PMA-12 equipped with an integrated sphere and a xenon lamp set at an excitation wavelength of λ_{ex} = 365 nm. To verify the accuracy of the system, Coumarin 6 (standard QY of 78%) and Rhodamine B (standard QY of 68%) were measured in ethanol, returning QY values of 78% and 66%, respectively.

■ RESULTS AND DISCUSSION

Each $CH_3NH_3PbBr_xI_{3-x}$ perovskite composition was obtained by combining equimolar ratios of PbX_2 and CH_3NH_3X (with X = Br, I) in DMF. EDX was used to confirm the final Pb:X ratios; 1.00:3.00 (±0.06) and 1.00:3.07 (±0.14) for the bromide- and iodide-based perovskite, respectively (Figure S2). The solutions were mixed with the mesoporous powders using vortex stirring at 2000 rpm for 30 min. After the solutions had thoroughly impregnated the pores, the powders were dried at 95 °C. The color of the powders changed within 5 min, as the solvent evaporated and the perovskites crystallized. The material was held at 95 °C for an additional 30 min to ensure complete evacuation of DMF from the pores. Qualitatively, the final color of each powder depended on the pore size of the template and the Br concentration, showing a clear spectral shift from black/brown to yellow/green as d_{pore} decreases and x increases (Figure 1). From the N_2 adsorption/desorption isotherm data, the average pore sizes are found to be $d_{pore} \approx 3.3, 3.7, 4.2, 6.2$, and 7.1 nm (Figure S1). The SAXS patterns (Figure 2a) of the templates containing $CH_3NH_3PbBr_3$ can be observed. The pores exhibited periodic, long-range ordering, with peaks indexed to the (10), (11), and (20) of a 2D hexagonal mesostructure ($P6mm$). The pore-to-pore distance is calculated from D = $2d_{10}/\sqrt{3}$, and the overall specifications for each template can be found in Table S1.

To determine whether the perovskite grows into the typical cubic phase in the presence of silica, we performed a Rietveld

Figure 1. Photographs of the mesoporous silica powders after impregnation and crystallization.
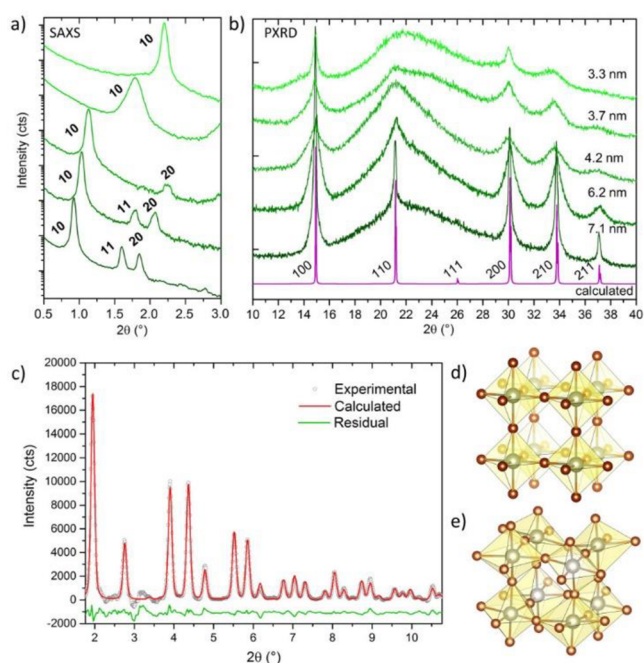

Figure 2. Structural analysis of the $CH_3NH_3PbBr_3$ perovskite. (a) SAXS patterns of the perovskite-impregnated silica templates match the $P6mm$ space group corresponding to the ordering of the mesopores. (b) PXRD patterns match the calculated pattern for the cubic ($Pm\overline{3}m$) structure. (c) Rietveld refinement of the synchrotron XRD data ($\lambda = 0.20196$ Å) obtained from the bulk perovskite/silica nanospheres system, confirming the cubic ($Pm\overline{3}m$) structure. Goodness-of-fit = 1.68, a = 5.9286(4) Å. Structural models of (d) the standard cubic structure compared to (e) the distorted cluster model. Note: the methylammonium ions were omitted from the models because of their negligible contribution to the X-ray scattering data.

refinement on synchrotron XRD data obtained on the bulk perovskite/silica nanosphere composite ($x = 3$). Figure 2c shows that the crystals grow into a typical $CH_3NH_3PbBr_3$ perovskite cubic phase ($Pm\overline{3}m$, a = 5.9286(4) Å). In conventional PXRD, the patterns of the perovskite nanocrystals inside the templates adopt the cubic crystal structure (Figure 2b), but gradual broadening of the Bragg peaks (e.g., 100 around 15°) is observed as the pore size decreases. Similar features could also be observed in the PXRD patterns for our $CH_3NH_3PbI_3$ samples (see Figure S3). Note that the broad

peak centered at around 22° is attributable to the amorphous SiO_2.

Although X-ray diffraction is sensitive to the crystallographic symmetry of the materials, much of the information on short to medium range ordering cannot be assessed from the Bragg peaks, especially in nanomaterials due to peak broadening. Pair distribution function (PDF) analysis is sensitive to the networks present in materials, and takes into account all the components of a sample including crystalline, nanocrystalline, and amorphous phases.[41] Using PDF, we can examine the local to intermediate range ordering of nanocrystals to clarify the structure and detect the presence of amorphous phases. PDF measurements on the bulk perovskite sample fit the cubic perovskite model very nicely (Figure S4a). On the other hand, PDF measurements on nanocrystal samples show some discrepancies (Figure S4b). For example, in the 3.3 nm template, the material has a broad peak at 6.32 Å with a shoulder around ~5.93 Å, indicating there are two different Pb−Pb nearest-neighbor distances. The typical $CH_3NH_3PbBr_3$ crystal has a lattice constant of ~5.93 Å, suggesting that the nanocrystals match the perovskite structure, but also has cells containing some expanded Pb−Pb distances or which possess a distorted structure. This was also observed at longer distances, such as the peak around 12 Å, explaining why the (100) peak in the PXRD becomes broad in the nanocrystalline systems (Figure 2a). To fit the PDF data we used the reverse Monte Carlo method assuming a ~2.3 nm $CH_3NH_3PbBr_3$ particle (Figure S4c). In this context, PDF is not used to determine the absolute structure, but as a comparative technique in combination with the PXRD data to conclude that the nanocrystals have a distorted perovskite network. A comparison between the $PbBr_6$ octahedra from the classic cubic structure and from the nanocluster model is shown in Figure 2d,e to highlight the distorted Pb−Br−Pb bonds (illustration of the whole cluster can be found in Figure S4d). Further details on these distortions will be reported in the future after performing additional PDF measurements.

Besides the broad peaks visible for all diffraction planes in the PXRD patterns, sharp peaks can also be specifically observed for the $\{h00\}$ reflections. This strongly suggests that the perovskite inside the channels grows along the $\langle 100 \rangle$ direction forming elongated crystals or nanorods. In order to separate the broader contributions from the sharp ones, the peaks were fitted by a double Gaussian function, and the Scherrer equation was used to estimate the average crystallite size in each sample (see Figure S5). Note that we used the peaks outside of the amorphous silica range, where the background could be subtracted clearly, and the results are reported in Table S1. For pore sizes ≤6.2 nm, the estimated crystallite sizes are 0.7−1.3 nm smaller than the pores. The ratio of spherical particles to nanorods is roughly estimated to be 5.1 ± 1.4, on the basis of the integrated Gaussian fit.

Transmission electron microscopy (TEM) was used to image the $CH_3NH_3PbBr_3$ and $CH_3NH_3PbI_3$ nanocrystals encapsulated in the silica templates. This class of perovskite is notoriously sensitive to electron beam damage, so the TEM micrographs were taken with great care to minimize the exposure/dwelling times and avoid changes in morphology. The HR-TEM images (Figure 3a−c) show the presence of a mixture of spherical and rod-shaped particles that extend across the width of the channels. The Fourier transform of the HR-TEM images shows that the lattice fringes match the $\{211\}$ and $\{200\}$ crystal plane (d_{211} = 2.68 ± 0.02 Å, d_{200} = 2.99 ± 0.02
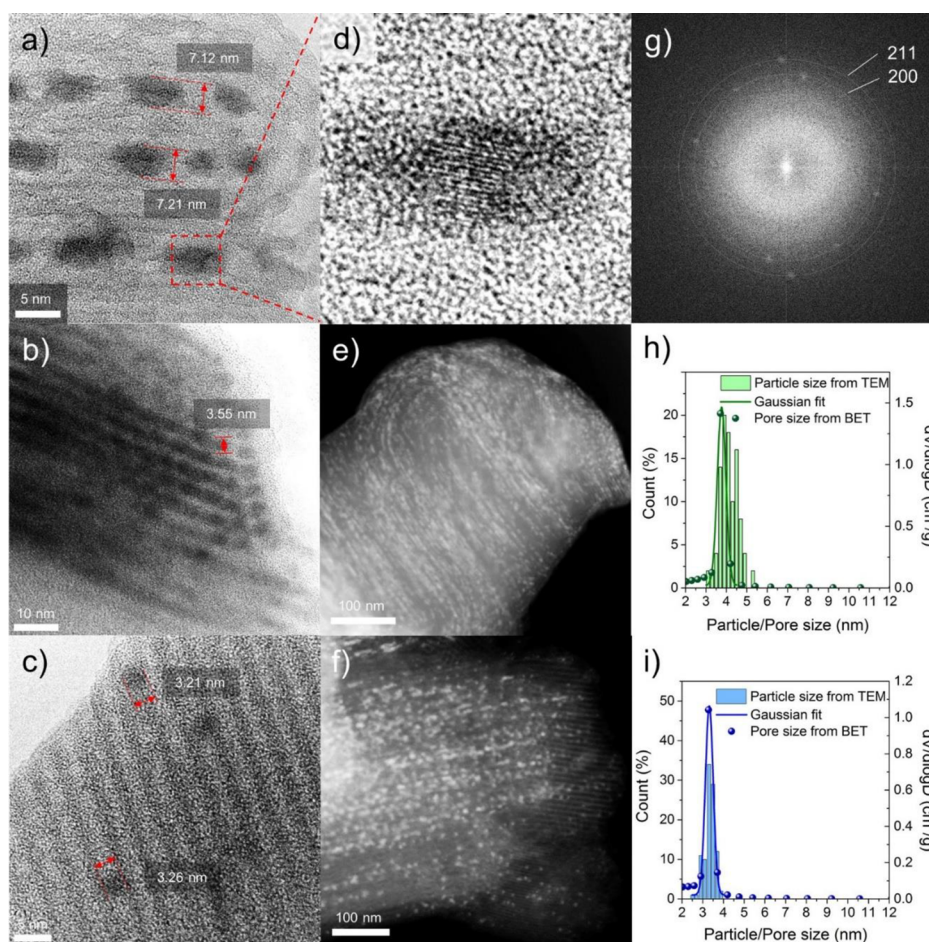
Figure 3. HR-TEM images of the $CH_3NH_3PbBr_xI_{3-x}$ perovskite/silica composite: (a) $x = 3$, $d_{pore} \sim 7.1$ nm; (b) $x = 0$, $d_{pore} \sim 3.7$ nm; (c) $x = 3$, $d_{pore} \sim 3.3$ nm. (d) Higher magnification centered on the selected area of the image displayed in part a and (g) its fast Fourier transform pattern. STEM images of the impregnated silica with (e) $d_{pore} \sim 3.7$ and (f) 3.3 nm for the bromide-based ($x = 3$) perovskite nanocrystals, along with the particle size distribution histograms (h and I, respectively) overlapping with the pore size distributions calculated from the N_2 sorption isotherms with the BJH method (including Gaussian fitting).

Å), with the latter being oriented along the direction of the channels (Figure 3d,g). Exposure to the electron beam did not affect the morphology of the nanocrystals, and the observed lattice parameter is far enough from the Pb{111} crystal plane ($d_{111} = 2.852$ Å), allowing us to rule out the possibility of electron-beam-induced chemical reduction or precipitation.[19] The preferential growth of nanorods along the ⟨001⟩ direction matches the PXRD data and has been previously reported for $CH_3NH_3PbBr_3$ nanowires.[42,43] The STEM images (Figure 3e,f) show that the nanocrystals are closely distributed along the channels and that the templates do not suffer from any deformation or collapsing (see Figure S6). For each sample, the crystallized perovskite was observed inside the templated channels, as clearly shown by the bright particles/nanorods that were aligned parallel to each other. The spherical nanoparticle and nanorod size distribution histograms (over 100 nanocrystals), measured on both HR-TEM and STEM micrographs, closely match pore size distribution of the mesoporous silica calculated from the isotherms with the Barrett−Joyner−Halenda (BJH) method.

Figure 4 shows the UV−Vis−NIR spectra for the different silica templates and the four compositions. The reflectance data is reported as absorption spectra to enable better comparison with the previous literature. The data provides a clear

measurement of the direct optical bandgap of the $CH_3NH_3PbBr_xI_{3-x}$ perovskites due to their sharp band edge. The bandgap energies measured for the various bulk compositions are similar to what was previously reported for comparable materials (the numerical values are reported in Table 1).[11,44] Small variations can be expected because the local crystal structure of hybrid perovskites is affected by the crystallinity and surface structure of the substrate.[8,33] The bulk samples include amorphous silica nanospheres to provide a similar perovskite/silica interface to the mesoporous templates. These measurements have no supplementary shoulder that would indicate the presence of both bulk and nanocrystals (example in Figure S7), confirming that the perovskite crystallized exclusively inside the mesopores and not at the surface of the grains. For each composition, a gradual shift of the band edge toward higher energies is an indication of how the bandgap increases due to confinement. With only four different compositions, one can easily cover the absorption spectrum from 1.52 to 2.62 eV with increments of less than 0.15 eV. The appearance of an excitonic peak is a signature of stronger electron−hole correlation as the crystal size is reduced. This feature appears to become more prominent as the Br content increases, to the point where a distinct exciton peak can be seen for the pure $CH_3NH_3PbBr_3$ even in the sample with 7.1

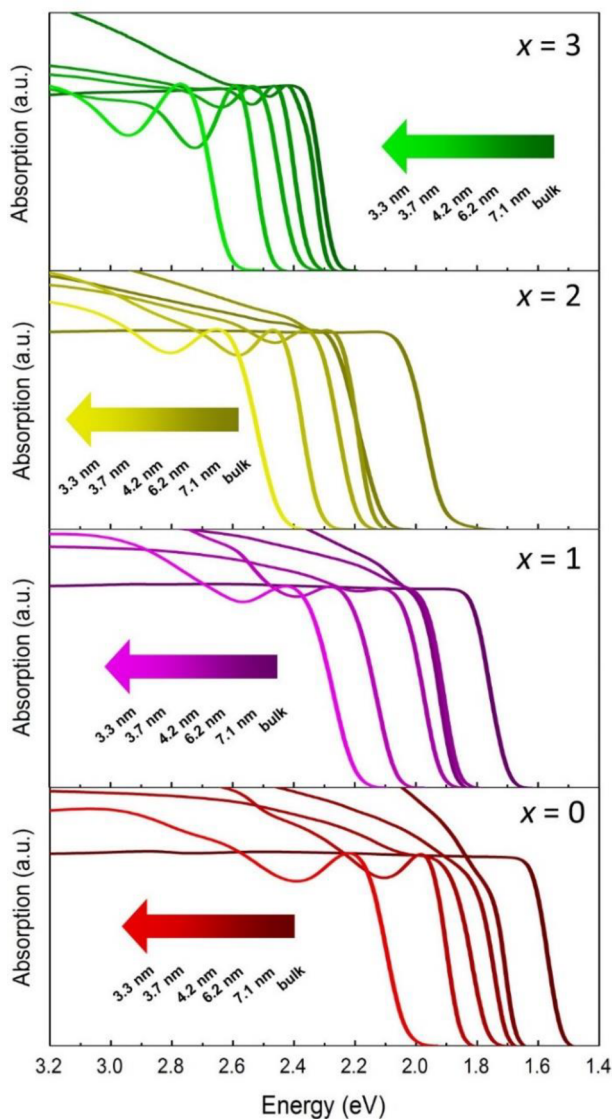**Figure 4.** UV−Vis−NIR absorption spectra (calculated from reflection measurements) for each $CH_3NH_3PbBr_xI_{3-x}$ (x = 0, 1, 2, 3) sample and mesoporous silica template.

Table 1. Bandgap Energies (in eV) Determined from the Cut-Off of the Absorption Band Edge Observed in Figure 4 for Each $CH_3NH_3PbBr_xI_{3-x}$ Composition and Pore Size[a]

pore size (nm)	x = 0	x = 1	x = 2	x = 3
∞	1.52 eV (0.03)	1.67 eV (0.10)	1.86 eV (0.14)	2.24 eV (0.07)
7.1	1.67 eV (0.05)	1.86 eV (0.11)	2.07 eV (0.13)	2.21 eV (0.04)
6.2	1.71 eV (0.06)	1.86 eV (0.08)	2.14 eV (0.10)	2.35 eV (0.06)
4.4	1.76 eV (0.10)	1.92 eV (0.12)	2.19 eV (0.11)	2.39 eV (0.08)
3.7	1.90 eV (0.06)	2.11 eV (0.20)	2.31 eV (0.10)	2.44 eV (0.07)
3.3	2.22 eV (0.12)	2.28 eV (0.21)	2.48 eV (0.23)	2.62 eV (0.13)

[a]The values in parentheses correspond to the Stokes shifts ΔE_{St}.

nm pore size. This could result from the fact that the exciton binding energy of the bromide-based perovskite is considerably

higher than for the iodide-based one.[25] The slope of the band edge remains mostly unchanged.

The Stokes shifts (ΔE_{St}, Table 1) obtained from comparing the absorption with the PL spectra (Figure 5a and Figure S8)
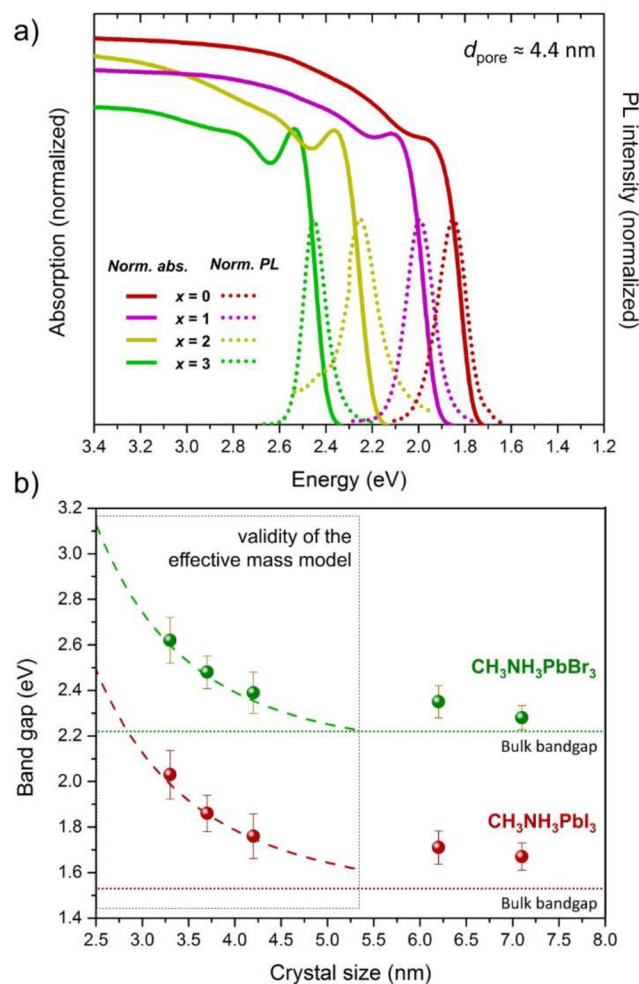

Figure 5. (a) Absorption (solid lines) and PL spectra (dotted lines) for each perovskite composition impregnated in mesoporous silica with d_{pore} ≈ 4.2 nm (see Figure S8 for other pore sizes). (b) Bandgap in function of the crystal/pore size for the iodide- and bromide-based hybrid perovskites, along with the expected trend calculated from the effective mass model for 1D structures. The dotted lines corresponds to the bandgap of the bulk samples.

tend to be smaller for the pure halide composition (x = 0 or 3). For the intermediate compositions, a light-soaking experiment resulting in gradual appearance of a new PL peak in the bulk perovskite and in the templates with larger pores (see Figure S9) confirms that the materials undergo phase segregation under light exposure, leading to the presence of instable Br- and I-rich microdomains,[11] contributing to the overall crystal disorder and resulting in a notably larger ΔE_{St}. We can observe that the Stokes shift also increases significantly for the templates with 3.3 nm pore size compared to the other templates. In addition, the PL emission spectra of the intermediate composition x = 2 reveal a split peak for d_{pore} ≈ ∞, 7.1, and 6.2 nm, suggesting the coexistence of two phases (Figure S8). It should be noted, however, that while the smaller peak seems to match the position of the absorption band edge, and thus reflects the presence of a phase with the expected

stoichiometry, a second peak is located in the I-rich region for $d_{pore} \approx \infty$ and in the Br-rich region for $d_{pore} \approx 7.1$ and 6.2 nm. Also, below $d_{pore} \approx 4.2$ nm, only one phase, matching the absorption band edge, appears to be emitting (Figure 5a and Figure S8). Not only do these results support what has been previously reported on the formation of microdomains, they also suggest that spatially confining the perovskite crystals within static and inert walls has the potential to limit the degree of structural disorder responsible for certain stability issues.

The measured bandgaps for $x = 0$ and 3 were plotted against their respective crystal size (Figure 5b), highlighting the gradual displacement of their respective conduction and valence bands. To model quantum confinement in the nanoparticles, we plotted a simplified particle-in-a-box model for $CH_3NH_3PbBr_3$ and $CH_3NH_3PbI_3$, taking into account Coulombic interactions and the first zero point of the cylindrical Bessel function (see details in the Supporting Information). An approximation using cylindrical 1D structure is used here because we assume that, in addition to the significant proportion of rod-shaped particles, most of the nanocrystals are packed closely and are expected to behave as a 1D structure. Moreover, the asymmetry in the electronic environment (air vs SiO_2) might also promote this effect. This model fits best for the smaller pore sizes (3.3−4.2 nm). However, even if the confinement energy is known to be more accurate for larger particles, the electrostatic term can quickly diverge when the size of the nanocrystals increases above the Bohr radius, especially for materials with small dielectric constants.[45] According to previous reports, the positions of the bandgaps measured for the smallest crystal with $x = 0$ and 3 are comparable to nanoplatelets with 3−4 atomic layers.[17,18,22]

The pure bromide composition ($x = 3$), unlike the others, is characterized by strongly emissive PL. Figure 6a clearly highlights the gradual shift of the emission from green to blue as the pore size is decreased, along with a significant peak broadening. We suspect that the increase in peak width might be caused by crystal distortion assessed by the PDF analysis for the smaller particles, although it did not seem to affect the bandgap (as confirmed by the effective mass model). On the other hand, the PL lifetime tends to decrease with the pore size (Figure 6b), and the QY of the bulk reaches 7.2% while that of the composites remain relatively low (<5.5%) (Table S2). Even though previously reported $CH_3NH_3PbBr_3$ nanoparticles of size ranging from 6 to 8 nm reported PL quantum efficiencies up to 83%,[46,47] it has been proposed that unpassivated crystals tend to exhibit lower emission yield.[48] The role of localized surface states is especially important in nanocrystals, and in $CH_3NH_3PbBr_xI_{3-x}$ perovskites this occurs mostly as vacancies and substitutions. The shorter lifetimes could be the result of dominant surface trapping as the crystal size decreases. In such cases, we can surmise that the surfaces in contact with the silanol groups and/or air are not effectively passivated and thus cannot prevent nonradiative recombination through localized states.

Exposing these perovskite samples to UV light can potentially affect their response. The stability of each sample was studied by comparing the PL lifetime of the pure iodide- and pure bromide-based samples before and after UV irradiation exposure, as well as after an overnight recovery period in the dark (Figures S10−S11). The bulk samples were strongly affected by UV light, causing their lifetimes to decrease by factors of 13 and 8 for $x = 0$ and $x = 3$, respectively. There was very little recovery after UV irradiation of the bulk samples.
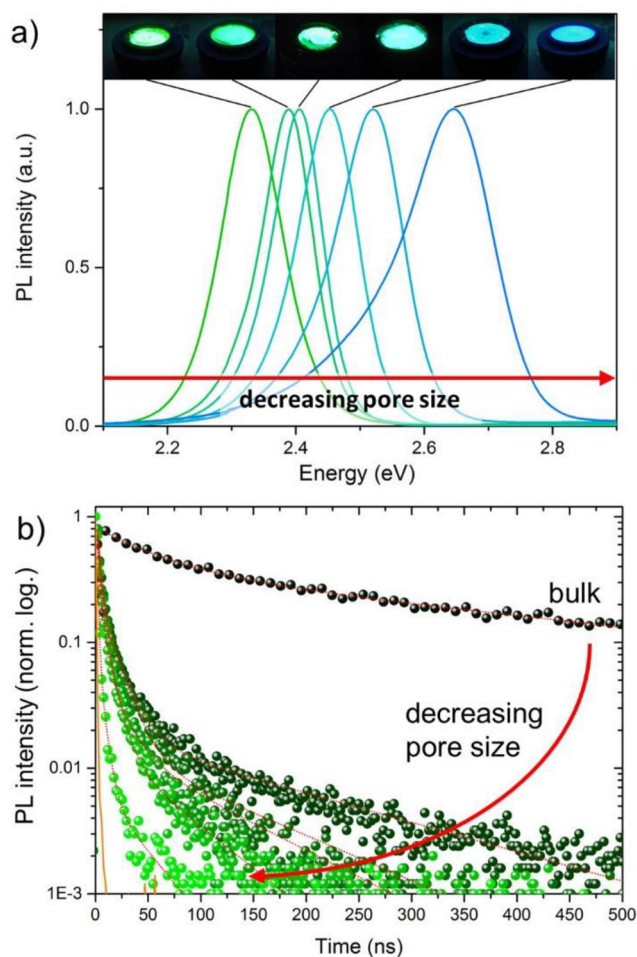

Figure 6. (a) Photographs and PL spectra of $CH_3NH_3PbBr_3$ impregnated in the various silica template (from bulk on the left to $d_{pore} \approx 3.3$ nm on the right) under black light ($\lambda = 364$ nm). (b) PL decays measured for $CH_3NH_3PbBr_3$ impregnated in the various silica template (green) along with their respective triple exponential fitting (red dotted curves). The orange curve represents the IRF.

The overall lifetime of the composite samples consistently decreased with crystal size, but the resting period resulted in the complete restoration, and in some cases improvement, of the optical properties, highlighting its strong resistance to UV irradiation. The PL decays best fit to triple exponential functions, so the exact mechanisms responsible for radiative recombination are difficult to discern here. These results, however, support once more the idea that confining $CH_3NH_3PbX_3$ crystals in a rigid template protects the structure from various types of degradation. It is possible that the energy imparted by UV exposure triggers two interrelated processes: (1) ion migration (mostly halide) and (2) annealing of the sample. In bulk samples, ion migration can drive the components of the perovskite relatively far apart from their original location, explaining why the crystal might remain highly contorted even after recovery. The "rigid" spatial confinement provided by the template could limit how far the constituents can migrate, so the system can eventually return to its original equilibrium state after the recovery period.

■ CONCLUSION

In summary, we have successfully synthesized CH_3NH_3-$PbBr_xI_{3-x}$ nanocrystals embedded in mesoporous silica

templates. We show that the crystal size matches the pore size distribution and that the crystal structure is maintained even for particles down to 3.3 nm in diameter, although with slight distortions. TEM and X-ray diffraction data show the samples are a mixture of spherical and rod-shaped particles enclosed in the silica channels. Our optical measurements show that both the Br content and the size-dependent confinement are directly related to the bandgap. The gradual shift of the photoluminescence from green to blue (for the bromide-based perovskite) is additional evidence that fine-tuning of the optical properties can be obtained from simply controlling the pore size of the template. A simplified particle-in-a-box model for 1D structures could fit the confinement of the smaller quantum dots (<4.2 nm) nicely, but fails for the bigger crystals due to the model's limitations. Because of their structural disorder, intermediate compositions also show larger Stokes shift values. The PL lifetime was directly dependent on crystal size, suggesting that localized surface states might induce non-radiative recombination pathways. Additionally, confining the crystals inside a rigid matrix such as mesoporous silica likely helps protect the structure from being damaged by UV irradiation. Our experimental procedure is simple and scalable; the results are proof of true quantum confinement and also showcase improved structural stability. For these reasons, we believe that this work will pave the way for extensive research on the topic, and ultimately find appropriate implementation in optoelectronic applications.

■ ASSOCIATED CONTENT

Ⓢ Supporting Information

The Supporting Information is available free of charge on the ACS Publications website at DOI: 10.1021/jacs.6b05608.

> Detailed characterization of each perovskite composition impregnated in mesoporous silica, PDF data, EDX and XRD patterns, high-magnification STEM of empty and impregnated host templates, absorption and PL spectra, light-soaking effect, PL lifetime measurements, and confinement model calculations (PDF)

■ AUTHOR INFORMATION

Corresponding Author

*Yamauchi.Yusuke@nims.go.jp

Notes

The authors declare no competing financial interest.

■ ACKNOWLEDGMENTS

■ REFERENCES

(1) Ponseca, C. S., Jr.; Savenije, T. J.; Abdellah, M.; Zheng, K.; Yartsev, A.; Pascher, T.; Harlang, T.; Chabera, P.; Pullerits, T.; Stepanov, A.; Wolf, J. P.; Sundström, V. *J. Am. Chem. Soc.* **2014**, *136*, 5189.

(2) Wehrenfennig, C.; Eperon, G. E.; Johnston, M. B.; Snaith, H. J.; Herz, L. M. *Adv. Mater.* **2014**, *26*, 1584.

(3) Xing, G.; Mathews, N.; Sun, S.; Lim, S. S.; Lam, Y. M.; Grätzel, M.; Mhaisalkar, S.; Sum, T. C. *Science* **2013**, *342*, 344.

(4) Stranks, S. D.; Eperon, G. E.; Grancini, G.; Menelaou, C.; Alcocer, M. J. P.; Leijtens, T.; Herz, L. M.; Petrozza, A.; Snaith, H. J. *Science* **2013**, *342*, 341.

(5) Kojima, A.; Teshima, K.; Shirai, Y.; Miyasaka, T. *J. Am. Chem. Soc.* **2009**, *131*, 6050.

(6) Kim, H.-S.; Lee, C.-R.; Im, J.-H.; Lee, K.-B.; Moehl, T.; Marchioro, A.; Moon, S.-J.; Humphry-Baker, R.; Yum, J.-H.; Moser, J. E.; Grätzel, M.; Park, N.-G. *Sci. Rep.* **2012**, *2*, 591.

(7) Lee, M. M.; Teuscher, J.; Miyasaka, T.; Murakami, T. N.; Snaith, H. J. *Science* **2012**, *338*, 643.

(8) Burschka, J.; Pellet, N.; Moon, S.-J.; Humphry-Baker, R.; Gao, P.; Nazeeruddin, M. K.; Grätzel, M. *Nature* **2013**, *499*, 316.

(9) Yang, W. S.; Noh, J. H.; Jeon, N. J.; Kim, Y. C.; Ryu, S.; Seo, J.; Seok, S. I. *Science* **2015**, *348*, 1234.

(10) Stoumpos, C. C.; Malliakas, C. D.; Kanatzidis, M. G. *Inorg. Chem.* **2013**, *52*, 9019.

(11) Hoke, E. T.; Slotcavage, D. J.; Dohner, E. R.; Bowring, A. R.; Karunadasa, H. I.; McGehee, M. D. *Chem. Sci.* **2015**, *6*, 613.

(12) Nozik, A. J.; Beard, M. C.; Luther, J. M.; Law, M.; Ellingson, R. J.; Johnson, J. C. *Chem. Rev.* **2010**, *110*, 6873.

(13) Yoffe, A. D. *Adv. Phys.* **2001**, *50*, 1.

(14) Kovalenko, M. V.; Manna, L.; Cabot, A.; Hens, Z.; Talapin, D. V.; Kagan, C. R.; Klimov, V. I.; Rogach, A. L.; Reiss, P.; Milliron, D. J.; Guyot-Sionnnest, P.; Konstantatos, G.; Parak, W. J.; Hyeon, T.; Korgel, B. A.; Murray, C. B.; Heiss, W. *ACS Nano* **2015**, *9*, 1012.

(15) Kim, B. H.; Hackett, M. J.; Park, J.; Hyeon, T. *Chem. Mater.* **2014**, *26*, 59.

(16) Ha, S. T.; Liu, X.; Zhang, Q.; Giovanni, D.; Sum, T. C.; Xiong, Q. *Adv. Opt. Mater.* **2014**, *2*, 838.

(17) Tyagi, P.; Arveson, S. M.; Tisdale, W. A. *J. Phys. Chem. Lett.* **2015**, *6*, 1911.

(18) Sichert, J. A.; Tong, Y.; Mutz, N.; Vollmer, M.; Fischer, S.; Milowska, K. Z.; García Cortadella, R.; Nickel, B.; Cardenas-Daw, C.; Stolarczyk, J. K.; Urban, A. S.; Feldmann, J. *Nano Lett.* **2015**, *15*, 6521.

(19) Dou, L.; Wong, A. B.; Yu, Y.; Lai, M.; Kornienko, N.; Eaton, S. W.; Fu, A.; Bischak, C. G.; Ma, J.; Ding, T.; Ginsberg, N. S.; Wang, L.-W.; Alivisatos, A. P.; Yang, P. *Science* **2015**, *349*, 1518.

(20) Schmidt, L. C.; Pertegás, A.; González-Carrero, S.; Malinkiewicz, O.; Agouram, S.; Mínguez Espallargas, G.; Bolink, H. J.; Galian, R. E.; Pérez-Prieto, J. *J. Am. Chem. Soc.* **2014**, *136*, 850.

(21) Zhang, F.; Zhong, H.; Chen, C.; Wu, X.-G.; Hu, X.; Huang, H.; Han, J.; Zou, B.; Dong, Y. *ACS Nano* **2015**, *9*, 4533.

(22) Hassan, Y.; Song, Y.; Pensack, R. D.; Abdelrahman, A. I.; Kobayashi, Y.; Winnik, M. A.; Scholes, G. D. *Adv. Mater.* **2016**, *28*, 566.

(23) Zheng, K.; Zhu, Q.; Abdellah, M.; Messing, M. E.; Zhang, W.; Generalov, A.; Niu, Y.; Ribaud, L.; Canton, S. E.; Pullerits, T. *J. Phys. Chem. Lett.* **2015**, *6*, 2969.

(24) Longo, G.; Pertegás, A.; Martínez-Sarti, L.; Sessolo, M.; Bolink, H. J. *J. Mater. Chem. C* **2015**, *3*, 11286.

(25) Tanaka, K.; Takahashi, T.; Ban, T.; Kondo, T.; Uchida, K.; Miura, N. *Solid State Commun.* **2003**, *127*, 619.

(26) Chi, Y.-S.; Lin, H.-P.; Mou, C.-Y. *Appl. Catal., A* **2005**, *284*, 199.

(27) Chen, X.; Lam, K. F.; Zhang, Q.; Pan, B.; Arruebo, M.; Yeung, K. L. *J. Phys. Chem. C* **2009**, *113*, 9804.

(28) Vaishnavi, T. S.; Haridoss, P.; Vijayan, C. *Mater. Lett.* **2008**, *62*, 1649.

(29) Pellicer, E.; Rossinyol, E.; Rosado, M.; Guerrero, M.; Domingo-Roca, R.; Suriñach, S.; Castell, O.; Baró, M. D.; Roldán, M.; Sort, J. *J. Colloid Interface Sci.* **2013**, *407*, 47.

(30) Fukuoka, A.; Kimura, J.-i.; Oshio, T.; Sakamoto, Y.; Ichikawa, M. *J. Am. Chem. Soc.* **2007**, *129*, 10120.

(31) Lee, J. E.; Lee, N.; Kim, T.; Kim, J.; Hyeon, T. *Acc. Chem. Res.* **2011**, *44*, 893.

(32) Malgras, V.; Ataee-Esfahani, H.; Wang, H.; Jiang, B.; Li, C.; Wu, K. C.-W.; Kim, J. H.; Yamauchi, Y. *Adv. Mater.* **2016**, *28*, 993.

(33) Malgras, V.; Ji, Q.; Kamachi, Y.; Mori, T.; Shieh, F. K.; Wu, K. C.-W.; Ariga, K.; Yamauchi, Y. *Bull. Chem. Soc. Jpn.* **2015**, *88*, 1171.

(34) Nguyen, S. V.; Szabo, V.; On, D. T.; Kaliaguine, S. *Microporous Mesoporous Mater.* **2002**, *54*, 51.

(35) Wang, N.; Yu, X.; Wang, Y.; Chu, W.; Liu, M. *Catal. Today* **2013**, *212*, 98.

(36) Beck, J. S.; Vartuli, J. C.; Roth, W. J.; Leonowicz, M. E.; Kresge, C. T.; Schmitt, K. D.; Chu, C. T. W.; Olson, D. H.; Sheppard, E. W.; McCullen, S. B.; Higgins, J. B.; Schlenker, J. L. *J. Am. Chem. Soc.* **1992**, *114*, 10834.

(37) Zhao, D.; Feng, J.; Huo, Q.; Melosh, N.; Fredrickson, G. H.; Chmelka, B. F.; Stucky, G. D. *Science* **1998**, *279*, 548.

(38) Egami, T.; Billinge, S. J. L. *Underneath the Bragg Peaks: Structural Analysis of Complex Materials*; Pergamon Materials Series; Elsevier: Oxford, U.K., 2003.

(39) Barrett, E. P.; Joyner, L. G.; Halenda, P. P. *J. Am. Chem. Soc.* **1951**, *73*, 373.

(40) Storck, S.; Bretinger, H.; Maier, W. F. *Appl. Catal., A* **1998**, *174*, 137.

(41) Tominaka, S.; Yoshikawa, H.; Matsushita, Y.; Cheetham, A. K. *Mater. Horiz.* **2014**, *1*, 106.

(42) Wong, A. B.; Lai, M.; Eaton, S. W.; Yu, Y.; Lin, E.; Dou, L.; Fu, A.; Yang, P. *Nano Lett.* **2015**, *15*, 5519.

(43) Teunis, M. B.; Jana, A.; Dutta, P.; Johnson, M. A.; Mandal, M.; Muhoberac, B. B.; Sardar, R. *Chem. Mater.* **2016**, *28*, 5043.

(44) Gil-Escrig, L.; Miquel-Sempere, A.; Sessolo, M.; Bolink, H. J. *J. Phys. Chem. Lett.* **2015**, *6*, 3743.

(45) Brus, L. E. *J. Chem. Phys.* **1984**, *80*, 4403.

(46) Gonzalez-Carrero, S.; Galian, R. E.; Pérez-Prieto, J. *J. Mater. Chem. A* **2015**, *3*, 9187.

(47) De Roo, J.; Ibáñez, M.; Geiregat, P.; Nedelcu, G.; Walravens, W.; Maes, J.; Martins, J. C.; Van Driessche, I.; Kovalenko, M. V.; Hens, Z. *ACS Nano* **2016**, *10*, 2071.

(48) Zheng, K.; Žídek, K.; Abdellah, M.; Messing, M. E.; Al-Marri, M. J.; Pullerits, T. *J. Phys. Chem. C* **2016**, *120*, 3077.